Open Ceramics 21 (2025) 100743

Contents lists available at ScienceDirect

Open Ceramics

journal homepage: www.sciencedirect.com/journal/open-ceramics

Spray drying granulation of potassium sodium niobate (KNN) for binder jetting: Feedstock preparation and influence on sintered material properties

Marco Mariani [a], Francesco Bertolini [a,*], Elisa Mercadelli [b], Guillermo Frias Blanco [c], Carlo Baldisserri [b], Antonio Javier Sanchez-Herencia [c], Carmen Galassi [a], Begoña Ferrari [c], Nora Lecis [a]

[a] Department of Mechanical Engineering, Politecnico di Milano, via La Masa 1, Milano, 20156, Italy
[b] Institute of Science, Technology and Sustainability for Ceramics, CNR-ISSMC, Via Granarolo 64, Faenza, 48018, Italy
[c] Instituto de Cerámica y Vidrio, CSIC-ICV, Calle Kelsen 5, Madrid, 28049, Spain

ARTICLE INFO

Keywords:
Binder jetting
Potassium sodium niobate
Spray drying granulation
Piezoceramic
Additive manufacturing

ABSTRACT

Binder jetting of potassium sodium niobate ($K_{0.5}Na_{0.5}NbO_3$) offers potential for generating shape-dependent responses with high industrial output. However, the printing stage relies heavily on the properties of the dry feedstock, making its performance optimization crucial. In this regard, morphological functionalization through granulation can be a useful methodology.

This study characterizes two powders in dry and wet states to develop colloidal suspensions for spray drying granulation. Particle size, shape, and ζ-potential are measured to stabilize them in an aqueous slurry. Granule morphology and flowability are assessed and compared with the original feedstock. Disk-shaped specimens are then printed and sintered.

Spray drying granulation successfully produces spherical and fine feedstocks compatible with the typical layer thickness (50 μm) of binder jetting. Densified parts displayed significant residual porosity (20–40 %) along the building direction, affecting piezoelectric performance: strain coefficients were reduced, but increased voltage coefficients yielded high figures-of-merit.

1. Introduction

Additive manufacturing of lead-free piezoceramics offers a novel method for crafting intricate functional components. Through innovative techniques like binder jetting (BJT) [1,2], stereolithography [3], direct ink writing [4] and selective laser sintering [5,6], intricate piezoceramic parts can be precisely fabricated with tailored properties. This approach brings about significant benefits including minimal material waste, extensive design freedom, and rapid prototyping capabilities. Lead-free compositions, such as potassium sodium niobate (KNN) and bismuth-based perovskites, are particularly gaining traction due to environmental concerns and regulatory constraints on lead-based materials [7]. With additive manufacturing, complex piezoceramic structures can be realized, opening up new avenues in sensor technology, actuation systems, and energy harvesting devices across a wide array of industries including electronics, aerospace, and healthcare [8–11].

Binder jetting is a widely utilized additive manufacturing method renowned for its versatility and efficacy in fabricating complex geometries across diverse sectors. However, employing binder jetting for ceramic powders presents distinct challenges, particularly concerning the formation and stability of the powder bed. Ceramic powders, unlike metallic or polymeric counterparts, often exhibit irregularities in particle size distribution, shape, and surface properties, complicating uniform layer deposition and subsequent consolidation. Additionally, the innate fragility and tendency to agglomerate further complicate matters, impeding the achievement of consistent part quality.

Overcoming the hurdles associated with powder bed formation in binder jetting for ceramic powders demands a comprehensive understanding of powder behaviour and the implementation of effective strategies for powder manipulation and control during the printing process. The simplest solution consists in the use of highly regular particles with micrometric size, which can be obtained from granulation techniques, as spray freezing or spray drying [12–14], or spheroidization processes at high temperatures [15,16], which can be inconvenient

* Corresponding author.
E-mail address: francesco.bertolini@polimi.it (F. Bertolini).

https://doi.org/10.1016/j.oceram.2025.100743
Received 31 October 2024; Received in revised form 29 December 2024; Accepted 23 January 2025
Available online 23 January 2025

in the case of complex compositions with volatile elements.

In a previous study [17], the effect of printing parameters on the formation and distribution of porosities, as well as their influence on piezoelectric properties, was investigated using non-granulated feedstock.

Building on these findings, the present work explores the intentional modulation of porosities through granulated feedstock, aiming to define a target density range and evaluate the corresponding variations in piezoelectric performance.The research focuses on optimizing both the preparation of colloidal suspensions and the granulation process for KNN, with the goal of offering a thorough protocol for producing powders ready for printing regardless of the feedstock supplier. Subsequently, printing tests are performed with the prepared feedstock to identify the granule characteristics that have the most significant impact on achieving successful densification and optimal piezoelectric performance.

2. Materials and methods

2.1. Dry powders analysis

For this investigation, $(K_{0.5}Na_{0.5})NbO_3$ (99 % purity) commercial powder from American Elements was employed.

The number-based particle size distribution (PSD) was determined using static image technique (Morphologi 4 granulometer, Malvern Instruments Ltd., UK). Specific surface area (SSA) of the raw material was determined via N_2 adsorption analysis (Monosorb Surface Area picnometer, Quantachrome Corporation, USA). The particle morphology of both raw material and granulated powder was analysed using FE-SEM (Sigma 500 microscope, ZEISS GmbH, Germany).

The crystalline phase of powders was assessed by x-ray diffractometry (Rigaku Smartlab SE, Tokyo, Japan): the signal was measured using Cu-Kα source from 20° to 80° with a scanning speed of 1° min^{-1}. The phases identification was performed by comparing the peaks position to the structure files COD DB #2,300,499 and COD DB #8,101,301 for the orthorhombic $K_{0.5}Na_{0.5}NbO_3$ and $K_6Nb_{10.8}O_{30}$ (KN), respectively.

The flowability of the powders (pre-heated at 60 °C to partially remove humidity) was measured as described in [13]. This procedure allows to estimate the actual flow of material from the powder hopper during the printing process and it is more reliable than conventional rheometry measurements, especially in the case of fine powders that tend to aggregate easily.

2.2. Colloidal suspension optimization

The preparation of suspensions with varying solid loadings was obtained by mixing the powders with deionized water and polyethyleneimine (PEI, MW 25,000, Sigma Aldrich, Germany), serving as a dispersant and binder for granulation purposes. The pH of these suspensions was adjusted using either tetramethylammonium hydroxide (TMAH) for pH above 8 or nitric acid (HNO_3) for pH below 6.

Dilute suspensions (1 g l^{-1}) were produced through mechanical stirring, while concentrated ones (20 vol.% of solid in liquid) underwent ball milling (G90 Jar Mill, Gladstone Engineering Co Ltd., UK) using alumina balls (5 mm diameter) as milling media. A 1:1:1 vol ratio of balls-to-suspension-to-air was maintained during milling. Milling was conducted for 60 min at a rotation speed of 350 rpm.

Surface charge of initial particles in water suspensions was evaluated by varying pH level between 4 and 12 using ζ-potential measurement (Zetasizer Nano ZS, Malvern Instruments Ltd., UK). This assessment was repeated after the addition of PEI dispersant at concentrations ranging from 0.3 to 5.0 wt.% to a suspension with pH = 10.

Solubility of KNN in water was examined under different conditions by:

- monitoring electrical conductivity of diluted suspensions at pH levels of 4, 6, 8, 10, and 12;
- determining concentrations of ionic species (K^+, Na^+, Nb^{3+}) in the supernatant from filtered suspensions after 7 days of stirring, with solid concentrations of 1 g l^{-1}, pH = 10 and varying PEI concentrations (0 to 5.0 wt.%), using induced-coupled plasma (ICP) analysis.

2.3. Granulation by spray drying

Suspensions with 20 vol.% solid loading and 3.0 wt.% of PEI relative to the solid loading underwent granulation through spray drying. Granulation was executed using a spray-drier (NIRO® MOBILE MINOR granulometer, GEA, Germany) with a two-fluid nozzle operating in top feed and co-current mode, featuring an internal diameter of 0.5 mm and compressed air at 1.2 bar The flow rate was maintained at a constant flow of 15 mL min^{-1} with slight adjustments necessary to ensure constant droplet formation and prevent nozzle blockages. Granulated particles were collected using a cyclone configuration particle collector. Inlet and outlet temperatures were regulated at 205 °C and 140 °C, respectively.

2.4. Printing and densification

The granulated powder was employed as feedstock material to produce cylindrical components by binder jetting 3D printing (Innovent+ 3D printer, ExOne, US). The process relies on the subsequent deposition of a polymeric binder onto a powder bed until the part is completed. The powder deposition and spreading parameters were optimised for each feedstock, while the layer thickness was kept fixed at 50 μm. The sample printed were disks with diameter $d = 15.80 \pm 0.04$ mm and thickness $s = 2.82 \pm 0.02$ mm and 3 repetitions were made for each condition.

Two different printing conditions were evaluated: one (P1) with lower binder saturation (BS) and gentler drying conditions, and the other (P2) with higher BS but harsher drying conditions. The first condition (P1) aimed at providing higher density, although it may lead to defects, while the second condition (P2) resulted in lower green density but more accurate printing [17]. The two conditions are detailed in Table 1.

The powder bed was cured at 180 °C for 6 h to crosslink the polyethylene glycol (PEG) based binder (AquaFuse – BA005, ExOne, US) and obtain the green specimens by manual brushing depowdering. The green parts were debinded to burn out all the polymer and then sintered for consolidation and densification. Sintering for both printing conditions was performed in a sealed alumina crucible surrounded by atmospheric KNN powder with 2 wt.% excess alkali.

The initial sintering cycle (T1) included debinding at 470 °C for 2 h at 5 °C min^{-1} and densification at 1130 °C for 2 h at a rate of 2.5 °C min^{-1}. After observing the superior results of the second printing condition (P2), an additional comparison was made using a second sintering cycle (T2), in an attempt to maximise the density achievable without considering the possible negative influence on the piezoelectric properties. This cycle followed the same debinding conditions as T1 but with densification at 1160 °C for 1 hour at 7.5 °C min^{-1}. The two cycles are shown in Fig. 1.

2.5. Characterization of the sintered samples

At each stage of the process, the geometry of the parts was measured with a digital calliper and the density was calculated by geometrical

Table 1
Printing parameters employed in the tested conditions.

	Binder Saturation (BS) [%]	Drying Time (DT) [s]	Target Bed Temperature (TBT) [°C]
P1	110	6	40
P2	130	14	60

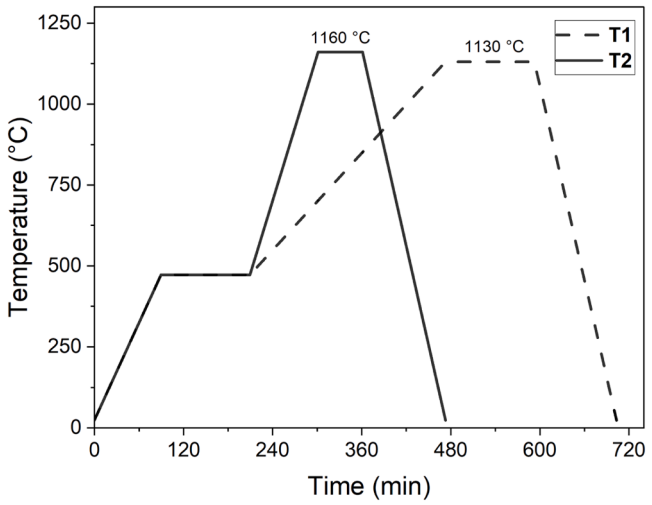

Fig. 1. Representation of the thermal cycles carried out in this study.

method, considering a theoretical full density value of 4.5 g cm^{-3}.

Microstructural features, as pores and grains size and distributions, were observed by FE-SEM along the cross section of the specimens.

Dielectric and piezoelectric properties were examined after sputtering Ag electrodes onto each face of KNN disks after polishing ($d = 10–11$ mm, s ~ 0.09*d), poling at 3 kV mm^{-1} at 120 °C for 40 min by capturing room-temperature piezoresonance spectra using an impedance analyser (Newton4 PSM 3750/IAI2 system, UK), and detecting resonance and antiresonance frequencies across the 100 Hz–40 MHz range. Room-temperature capacitance and loss tangent were measured at 1 kHz using the same equipment. The d_{33} piezoelectric charge coefficient constants were determined using a d_{33}-meter (S5865, Sinocera, China). Dielectric and piezoelectric constants were derived from piezoresonance primary data using a MATLAB (MathWorks, US) routine, according to ANSI/IEEE Std 176–1987.

3. Results and discussion

3.1. Colloidal suspensions stabilization

As can be seen from Fig. 2, the starting powders seem to feature an ultrafine fraction combined with a coarser fraction (above 10 μm) constituted by cuboidal shaped particles and aggregates. The presence of nanometric and micrometric particles is confirmed by granulometric analysis in Fig. 5. A SSA value of 15.6 m^2 g^{-1} was measured for the starting KNN powder by N_2-adsorption measurements. On one hand, multimodality could be an advantage in terms of maximum packing of the powder; on the other hand, the ultrafine fraction may require a larger amount of dispersant to stabilise the suspensions.

XRD analysis revealed the presence of a sodium-deficient secondary fraction, likely due to partial volatilization during the calcination process. The faceted particles can be identified as the main phase (KNN), while the secondary phase (KN) has a more irregular surface.

KNN does not display an isoelectric point within the conditions tested, as can be seen in Fig. 3**A**, in accordance with previous studies [18–20]. For pH ≥ 6, ζ-potential stands below −40 mV with a significant decrease only under extremely basic conditions (pH = 12). It should also be noted that under highly acidic conditions (pH < 5), the KNN particles precipitate soon after introduction in water, thus favouring the design of a dispersion system with a cationic polyelectrolyte as PEI. The ζ-potential remained negative under all tested conditions also in the case of PEI addition, with a meaningful variation only at high concentrations of dispersant (≥ 2.5 wt.%). This could be due to the relevant presence of ultrafine particles with a large SSA that can adsorb a significant amount of PEI and still attract anionic species from the suspension.

The conductivities of the diluted suspensions were tested to preliminarily determine the effect of the studied conditions on the ionic species dissolution in water. The graph in Fig. 3**A** underlines that extremely acidic and basic conditions lead to conductivities above 1 mS cm^{-1}, therefore these conditions are detrimental to the compound stability. Nonetheless, it should be remembered that the conductivity of the suspension is intrinsically subject to increase under highly acidic and, in particular, basic conditions. A pH equal to 10 is the most conservative choice. It should be noted that the conductivity correlated to the dissolution mechanism occurred within 24 h in absence of dispersant is comparable to the values measured after 72 h in presence of PEI. In addition, an increase in PEI concentration leads to slightly higher conductivity.

KNN normally experiences leaching of ionic species, especially for the alkaline ions (K^+ and Na^+). As can be seen from the graph in Fig. 3**B**, alkali species dissolve consistently in suspension without PEI, in particular sodium. As expected, PEI adsorption on the particles surface benefits alkali stability, however, it should be noted that niobium goes from complete stability in absence of dispersant to dissolution degrees comparable to that of sodium and potassium. Most likely, the introduction of $(NH)^{n+}$ groups from PEI allows to stabilise the surface charge even in case of Nb^{n+} dissolution, while the shift from the surface charge equilibrium conditions was too large to occur in absence of dispersant. Therefore, niobium dissolution could be responsible for the slight increase in conductivity observed in suspension with increasing amount of dispersant. However, the analysis of this mechanism was not within the aim of the study, as it does not affect significantly the granulation process.

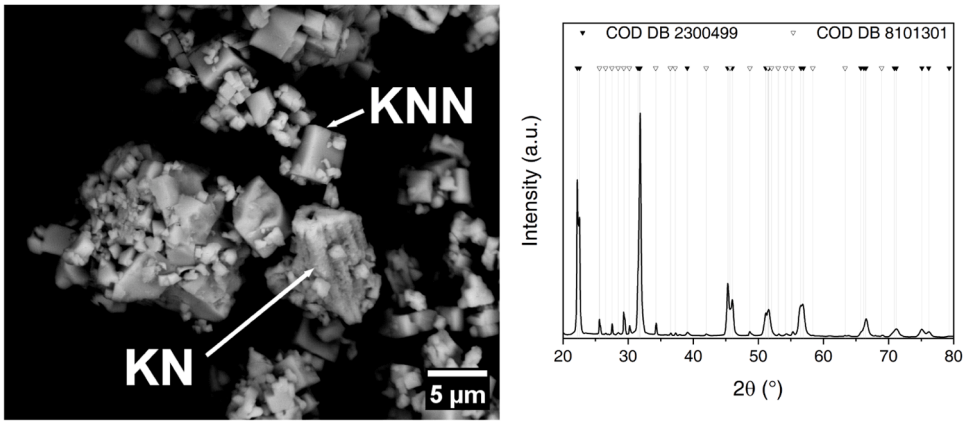

Fig. 2. SEM image and XRD graph of the raw materials with black (COD DB #2,300,499) and white (COD DB #8,101,301) ticks to identify the main KNN phase and the secondary KN phase, respectively.

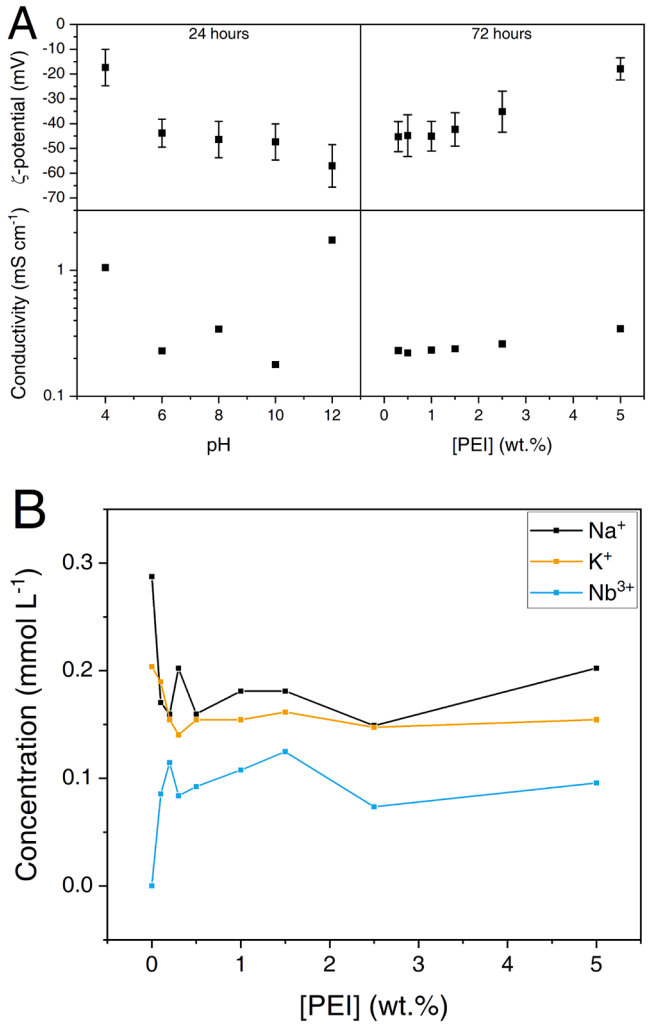

Fig. 3. Conditions to provide colloidal and chemical stability to the suspension for spray-drying: A) ζ-potential and conductivities of diluted suspensions (1 g l^{-1}) of KNN powder in water, measured at varying pH after 24 h and PEI concentrations after 72 h; B) Concentration values of ionic species in diluted suspensions (1 g l^{-1}) of KNN at varying concentrations of PEI in aqueous solution with a fixed pH of 10.

3.2. Spray drying granulation

A water-based suspension containing 1 wt.% of PEI as dispersant at pH = 10 was selected as starting point for the preparation of the slurry required for granulation. From previous studies [13], an additional amount of 2 wt.% of PEI was added to provide a sufficient amount of polymer which would act as the binding agent during the granules formation process. Finally, the particle solid loading was progressively increased to maximise its amount, while checking for the achievement of a suitable rheology for the process. As can be seen in Fig. 4, a solid loading of 20 vol.% provided a shear thinning effect up to at least $\gamma' = 1000\ s^{-1}$. The rheological behaviour is comparable to those of alumina-based suspensions (CT1200SG and BITOSSI) described in the previous study [13], which allowed to obtain satisfactory granulation processes, thus spray drying should lead to comparable results.

It can be observed in Fig. 5 that the spray drying process successfully produces spherical granules with an acceptable shape in most cases. Enlarged particles or platelets are rare to detect, thus the micrometric size detected by granulometry in the raw materials mostly corresponded to soft aggregates that were removed by stabilization in the colloidal suspension. Therefore, almost all granules have a regular shape (Fig. 5).

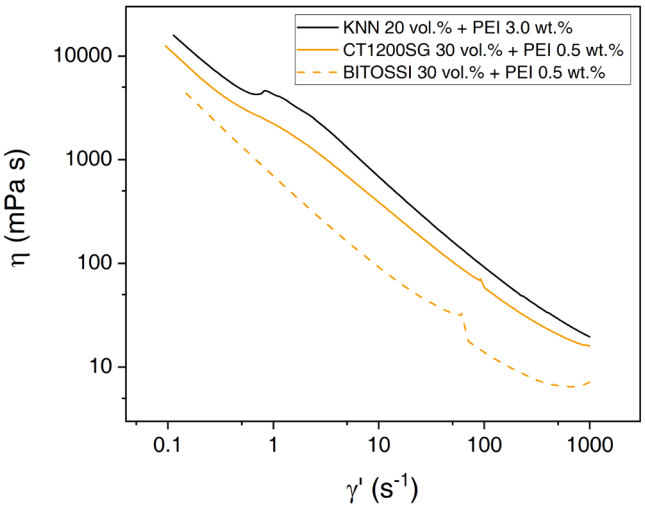

Fig. 4. Rheology curve (black) for a solid loading of 20 vol.% of KNN powder in water at pH = 10 with a total amount of PEI = 3.0 wt.%, compared to curves (yellow) of optimized slurries containing alumina stabilized with the same strategy in a previous study [13] employed in a spray drying process.

In this case, granulometry measurement reveals again a multimodal distribution: the main fraction corresponds to fine granules close to 1 μm, a secondary fraction is constituted by coarse granules (> 10 μm) and finally there are some unbonded ultrafine particles. Granulation led to a shift of the distribution peaks toward larger radii as expected.

As a consequence of the varied size distribution and granules shape, the flowability of the feedstock was improved. Indeed, the flows measured were equal to 168.8 ± 15.6 mg cm^{-2} s^{-1} and 197.3 ± 12.8 mg cm^{-2} s^{-1} (37.5 ± 3.5 mm^{-3} cm^{-2} s^{-1} and 43.8 ± 2.9 mm^{-3} cm^{-2} s^{-1}) for the raw and the granulated powder, respectively. The flowability of powder is sensitive to the aggregation of particles, which is dependent on short range interactions of electrostatic and capillary nature that are dependent on the radius-to-volume ratio. This is lowered with granulation, therefore interparticles interactions are weaker and the motion of the granules due to ultrasonic vibration is promoted. Consequently, the amount of material that can be deposited per unit of time is higher and the powder bed formation process can be accelerated. This result grants several advantages in the printing process, especially in terms of reduction of manufacturing time: the recoating and spreading operations are accelerated, thus the duration of the process is shortened.

3.3. Characterisation of density and microstructure of printed samples

The relative densities of the green parts produced using the granulated powder were slightly lower compared to those obtained with raw powder. Specifically, for P1 and P2, the values were 35.2 % and 31.0 %, respectively. This difference can likely be attributed to a lower powder bed density caused by the presence of hollow granules, which increased the overall porosity. The effect of the hollow granules appeared to outweigh the higher packing efficiency typically provided by larger, spherical particles.

The dimensional accuracy of the green parts compared to the CAD (Computer-Aided Design) model was satisfactory, with the diameter practically equal to the theoretical value (d = 15.75 mm), although an oversizing of 14 % was observed in both printing conditions for the thickness (s = 2.5 mm). P2 yielded the best results in terms of precision, with a standard deviation of 0.03 mm for diameter and 0.01 mm for thickness, indicating consistent and reliable part production. In contrast, P1 exhibited higher variability, with standard deviations of 0.13 mm for diameter and 0.06 mm for thickness, probably due to inadequate amount of binder deposited and drying conditions.

The lower green density resulted into lower densification after

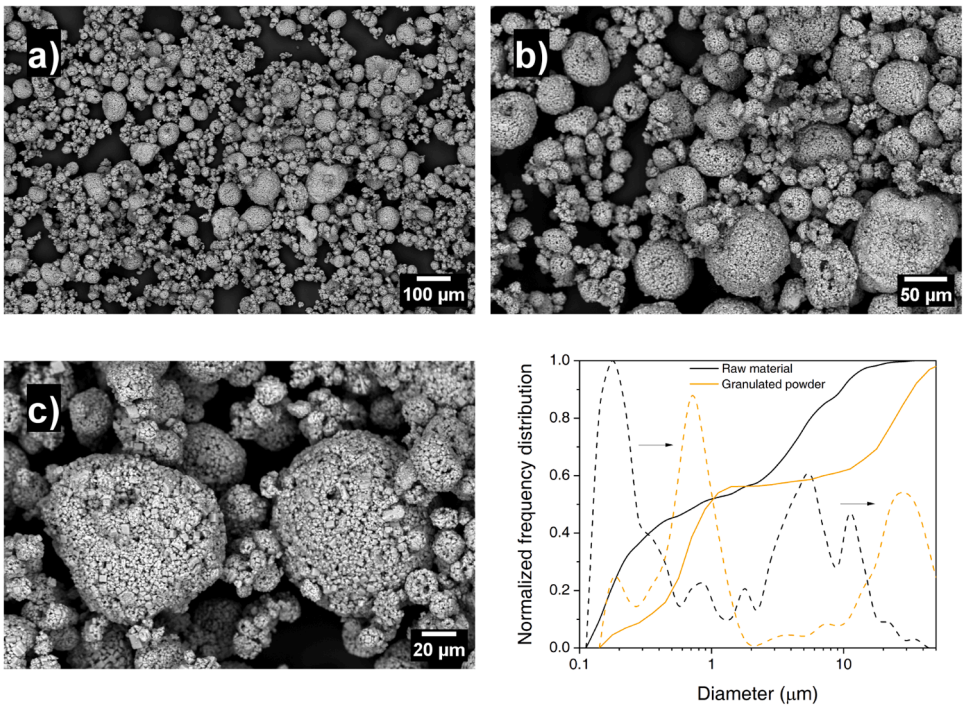

Fig. 5. SEM image of granulated powders, and particles size distribution curves before and after spray drying.

sintering, with relative densities of 62.4 % and 54.1 % for P1 and P2, respectively, when sintered at T1. These values, although consistent with expectations for the granulated feedstock, were lower compared to the densification achieved with the raw powder. The hollow nature of the granules impeded effective densification, limiting the contact points between particles and introducing pores that could not be fully eliminated during the sintering process. Compared to the raw powder, the difference is significant, with the raw powder reaching values of 74.7 % of the relative density. Even with T2 that reaches very high temperatures, the relative sintered density reaches quite low values of 72.9 %. Relative densities are shown in Fig. 6.

SEM images of both fracture and polished surfaces revealed a microstructure characterized by dense walls interrupted by closed pores (Fig. 7). For both P1_T1 and P2_T1, the distribution of porosity appeared homogeneous, and the pore sizes were comparable, despite the differences in printing conditions. In polished samples, areas where material successfully sintered displayed a uniform structure without microporosity, although pores of approximately tens of microns in size were observed, corresponding to the dimensions of the original granules.

A slight anisotropy in the porosity was also evident, with pores tending to align along the X-Y plane, following the layering direction. This was likely caused by binder deposition between layers, which did not uniformly infiltrate and crosslink, resulting in voids forming between successive layers.

For the samples sintered at T2 (Fig. 7**C**), this phenomenon was even more pronounced, with coalescence of pores into larger macropores, a behaviour not observed in parts printed with raw powder, where porosity was more uniformly distributed. Granules densified well in their outer shell where powder particles were in contact, but the inner regions of the granules did not close properly during the densification process. This led to a plateau in the overall densification, with maximum values reaching approximately 73–75 %, beyond which further densification was not possible.

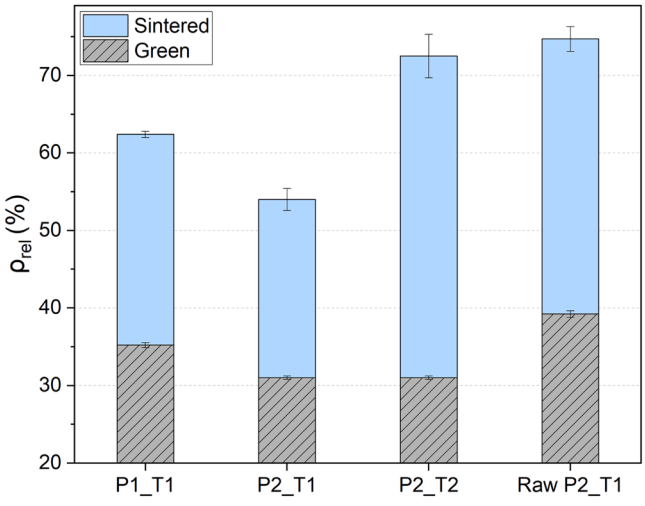

Fig. 6. Relative green and sintered densities of the printed samples compared to raw powder of a previous study [17].

3.4. *Piezoelectric characterisation*

The piezoelectric results are particularly interesting (Fig. 8 and Table 2), demonstrating that the use of granulated powders could be beneficial in the production of porous piezoceramics. Despite the inherent porosity introduced by the granules, the materials exhibited good piezoelectric responses comparable to those of denser samples, particularly for d_{33}.

The comparison between the two printing conditions shows that despite P2 displaying a higher overall porosity, it outperformed P1 in most piezoelectric parameters, except for the piezoelectric coefficient d_{31}. This result suggests that the printing parameters used in P1 are more appropriate to achieving favorable piezoelectric performance, possibly due to better distribution of the binder. A more in-depth discussion on the effect of printing parameters on piezoelectric properties can be found in another study [17].

The d_{33} coefficient, representing the piezoelectric charge response along the poling direction, exhibited values consistent with those typically observed in dense KNN samples, ranging from approximately 80 to

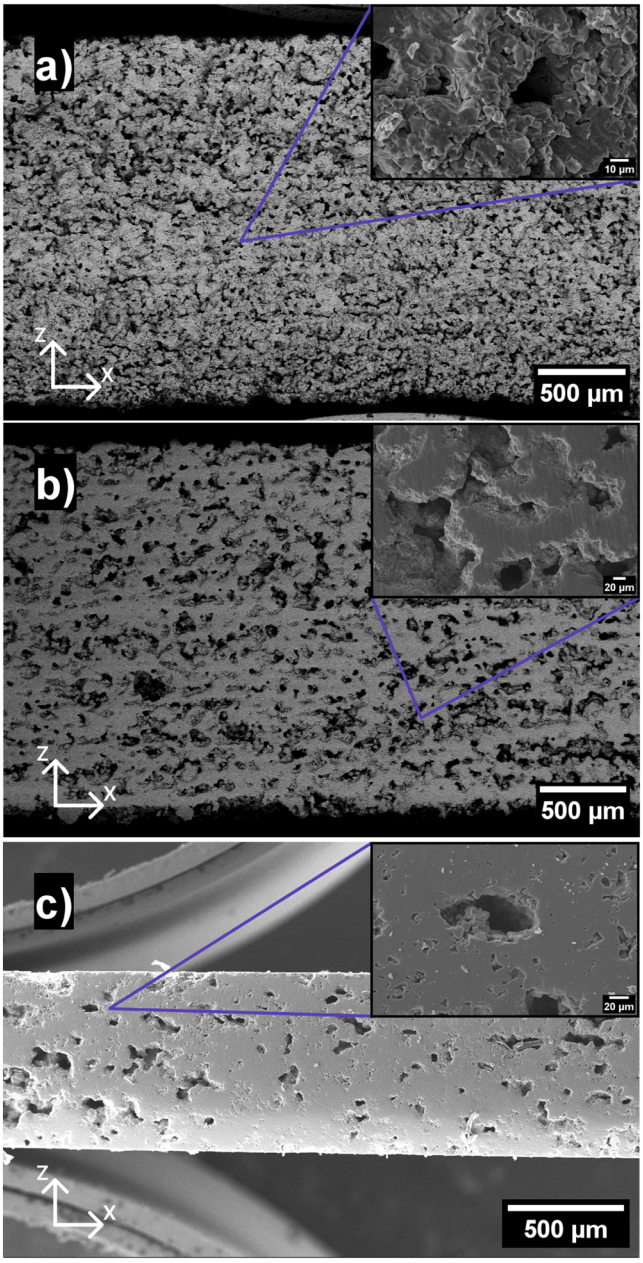

Fig. 7. SEM images of fracture surfaces of different samples: a) un-polished P1_T1; b) polished P2_T1, c) polished P2_T2.

120 pC N^{-1} [21,22]. Interestingly, this behavior appeared largely unaffected by the varying levels of porosity across the samples, suggesting that the d_{33} value is relatively insensitive to porosity within the examined density range. This finding aligns with previous studies [23,24], where it was shown that, in the relative density range of 50–90 %, d_{33} remains relatively stable or with slight decrease from the maximum. This stability is crucial for potential applications involving porous piezoceramics, where consistent piezoelectric performance is essential, regardless of the material's inherent porosity. A possible explanation for the retention of piezoelectric properties even at high porosity levels could be the maintenance of good connectivity between the KNN grains. This connectivity likely enables effective poling of all domains, preventing regions of unpolarized material. This observation suggests that the microstructure resulting from BJT printing is suitable for processing porous piezoelectric materials.

The g_{33} coefficient, which relates to the piezoelectric voltage response, exhibited favourable results for both sintering conditions of

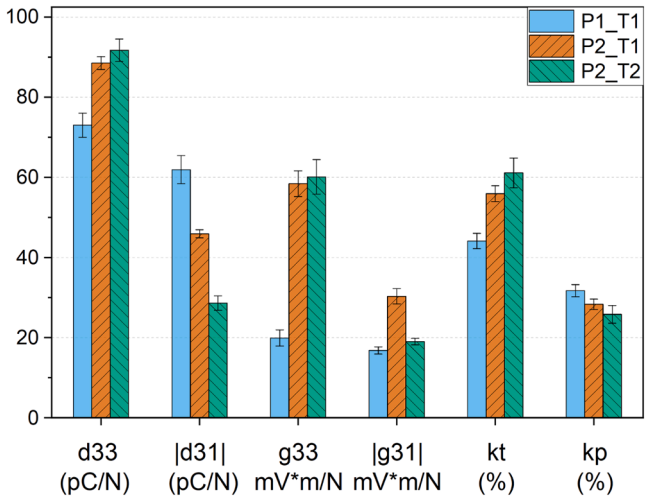

Fig. 8. Piezoelectric properties of sintered samples.

Table 2
Piezoelectric properties and Figures of Merits (FoM_s) of sintered samples.

	P1_T1	P2_T1	P2_T2
d_{33} (pC/N)	73 ± 2.1	88.5 ± 1.6	91.7 ± 2.8
$\|d_{31}\|$ (pC/N)	61.9 ± 2.6	45.9 ± 1	28.6 ± 1.2
g_{33} (mV*m/N)	19.9 ± 0.8	58.4 ± 3.2	60.1 ± 4.3
$\|g_{31}\|$ (mV*m/N)	16.8 ± 0.8	30.3 ± 0.9	19 ± 0.8
k_t (%)	44.1 ± 1.9	55.9 ± 2	61.1 ± 3.7
k_p (%)	31.7 ± 1.5	28.3 ± 1.3	25.8 ± 2.2
FoM_{33} [pm^2 N^{-1}]	1.45 ± 0.23	5.17 ± 0.35	5.5 ± 0.48
FoM_h [fm^2 N^{-1}]	701.6 ± 23.4	7.9 ± 3.6	756 ± 52.1

P2. The high level of porosity observed in these samples effectively reduced the dielectric constant, and when combined with a good d_{33}, resulted in elevated g_{33} values. This reduction in dielectric constant due to porosity is crucial in enhancing g_{33}, as it amplifies the voltage response generated per unit of mechanical stress.

These high g_{33} values are fundamental to achieving high figures of merit, particularly FoM_{33}, which is directly influenced by both the piezoelectric charge response and the reduced dielectric constant.

In contrast, P1, despite its lower density, showed unexpectedly low g_{33} values and high dielectric constant values. These results were comparable to those typically found in denser materials with about 80 % relative density.

The electromechanical coupling factor (k_{ij}) is a key indicator of the effectiveness with which a piezoelectric material converts electrical energy into mechanical energy, or vice versa. In this study, the thickness mode coupling factor (k_t) showed exceptional values across all samples, with the P2_T2 condition reaching an impressive 61.1 %, far exceeding the typical 46 % observed in pure KNN [25,26] and entering the range commonly associated with textured materials [27]. This increase in k_t strongly suggests the presence of anisotropy in the microstructure, likely induced by the binder jetting technique, as partially corroborated by SEM micrographs. However, this enhancement in k_t was accompanied by a notable decrease in the planar coupling factor (k_p), with values dropping below 30 %. This inverse relationship between k_t and k_p further confirms the anisotropic nature of the material, where the microstructural alignment introduced by the printing process favors energy conversion along the thickness direction but limits it in the planar direction.

The FoM_{33}, defined as the product of d_{33} and g_{33}, is a crucial parameter for evaluating materials in energy harvesting applications. For P1, the unexpectedly low g_{33} significantly compromised the overall FoM_{33}, resulting in a reduced figure of merit that limits its effectiveness for energy harvesting purposes (Table 2). Conversely, for both sintering

conditions of P2, the combination of a high d_{33} and elevated g_{33} yielded excellent FoM_{33} values, exceeding 5 $pm^2 N^{-1}$. These results highlight the potential of P2 procedure for energy harvesting, where a strong piezoelectric response and high voltage generation are critical.

On the other hand, the hydrostatic figure of merit ($FoM_h = (d_{33}+2\ d_{31})*(g_{33}+2\ g_{31})$) is particularly relevant for hydrostatic applications, such as underwater sensing or pressure detection, where decoupling the piezoelectric response along the 33 direction from the 31 direction is desired. This decoupling can be achieved by leveraging the porosity within the material. For P1_T1 and P2_T2, FoM_h values above 700 $fm^2 N^{-1}$ were obtained (Table 2), indicating effective decoupling and thus good suitability for hydrostatic applications. In contrast, for P2_T1, the FoM_h values were very low, comparable to those of dense materials ($d_{33} \sim 2|d_{31}|$), with little to no decoupling observed between the 33 and 31 responses.

4. Conclusions

In conclusion, spray drying granulation has proven to be an effective technique to enable the printing of powders with inherently low flowability, allowing for the fast production of porous materials. This method is particularly suitable for piezoelectric materials, where the presence of controlled porosity can enhance specific performance metrics.

The spray drying granulation process demonstrated its effectiveness in producing spherical and flowable KNN feedstock suitable for binder jetting. The granulated powders exhibited improved flowability compared to raw powders, enabling consistent powder bed formation during printing. However, the presence of hollow granules introduced significant porosity in the printed components, which had a pronounced effect on the final densification after sintering. Despite this, the microstructure generated through binder jetting showed notable anisotropy, as evidenced by the directional alignment of porosity and enhanced electromechanical coupling factors.

Despite the relatively high levels of porosity, the piezoelectric performance of the sintered components remained competitive. Specifically, the d_{33} values remained stable across varying porosity levels, suggesting that the connectivity between KNN grains was preserved and that the BJT technique is well-suited for processing porous piezoelectric materials.

Furthermore, the reduction in dielectric constant caused by the increased porosity contributed to high g_{33} values, resulting in excellent figures of merit (FoM_{33} and FoM_h). The electromechanical coupling factor k_t also reached values typically seen in textured materials, supporting the idea that the anisotropic microstructure generated by binder jetting favors energy conversion along the thickness direction.

The coefficient d_{33} maintained high levels despite the presence of porosities and combined with elevated values of g_{33} and the decoupling of d_{31} from d_{33}, resulted in excellent figures of merit (FoM_{33} *and* FoM_h).

Funding

This work was supported by the JECS Trust grant [Contract no. 2021268] and by the project PID2022–137274NB-C31 funded by AEI10.13039501100011033.

CRediT authorship contribution statement

Marco Mariani: Writing – review & editing, Writing – original draft, Visualization, Validation, Methodology, Investigation, Formal analysis, Data curation, Conceptualization. **Francesco Bertolini:** Writing – original draft, Visualization, Methodology, Investigation, Formal analysis, Data curation. **Elisa Mercadelli:** Writing – review & editing, Investigation, Formal analysis. **Guillermo Frias Blanco:** Methodology, Investigation. **Carlo Baldisserri:** Writing – review & editing, Investigation, Formal analysis. **Antonio Javier Sanchez-Herencia:** Supervision, Resources, Project administration, Conceptualization. **Carmen Galassi:** Writing – review & editing, Validation, Supervision. **Begoña Ferrari:** Writing – review & editing, Supervision, Resources, Project administration, Formal analysis, Conceptualization. **Nora Lecis:** Supervision, Resources, Project administration, Funding acquisition, Conceptualization.

Declaration of competing interest

The authors declare that they have no known competing financial interests or personal relationships that could have appeared to influence the work reported in this paper.

Acknowledgements

Authors would like to acknowledge JECS Trust for the short mobility funding that allowed to realise the project. MM also acknowledge the "Colloidal Processing" Laboratory of Instituto de Cerámica y Vidrio (ICV) where this research activity was developed.

The authors also acknowledge the "Functional Sintered Materials (Funtasma)" Interdepartmental Laboratory of Politecnico di Milano, where this research activity was partially developed.

References

[1] M. Mariani, E. Mercadelli, L. Cangini, C. Baldisserri, C. Galassi, C. Capiani, N. Lecis, Additive manufacturing of piezoelectric niobium-doped lead zirconate titanate (PZT-N) by binder jetting, Crystals 13 (2023) 883, https://doi.org/10.3390/cryst13060883.

[2] V. Sufiiarov, A. Kantyukov, A. Popovich, A. Sotov, Structure and properties of barium titanate lead-free piezoceramic manufactured by binder jetting process, Materials (Basel) 14 (2021) 4419, https://doi.org/10.3390/ma14164419.

[3] W. Chen, F. Wang, K. Yan, Y. Zhang, D. Wu, Micro-stereolithography of KNN-based lead-free piezoceramics, Ceram. Int. 45 (2019) 4880–4885, https://doi.org/10.1016/j.ceramint.2018.11.185.

[4] Y.Y. Li, L.T. Li, B. Li, Direct ink writing of 3-3 piezoelectric composite, J. Alloys Compd. 620 (2015) 125–128, https://doi.org/10.1016/j.jallcom.2014.09.124.

[5] L. Ji, Y. Jiang, Y. Gao, X. Du, Laser sintering effects on the physical properties and structure of 0.94(K0.5Na0.5)NbO3-0.06LiTaO3 lead-free piezoelectric ceramics, J. Laser Appl. 21 (2009) 124–128, https://doi.org/10.2351/1.3184430.

[6] D.M. Gureev, R.V. Ruzhechko, I.V. Shishkovskii, Selective laser sintering of PZT ceramic powders, Tech. Phys. Lett. 26 (2000) 262–264, https://doi.org/10.1134/1.1262811.

[7] RoHS Restricted Substances, RoHS Guid. (2020). https://www.rohsguide.com/rohs-substances.htm (accessed October 23, 2022).

[8] J.M. Rosso, E.A. Volnistem, I.A. Santos, T.G.M. Bonadio, V.F. Freitas, Lead-free NaNbO3-based ferroelectric perovskites and their polar polymer-ceramic composites: fundamentals and potentials for electronic and biomedical applications, Ceram. Int. 48 (2022) 19527–19541, https://doi.org/10.1016/j.ceramint.2022.04.089.

[9] J. Cheng, Y. Chen, J.W. Wu, X.R. Ji, S.H. Wu, 3d printing of BaTiO3 piezoelectric ceramics for a focused ultrasonic array, Sensors (Switzerland) 19 (2019), https://doi.org/10.3390/s19194078.

[10] J. Li, M. Yan, Y. Zhang, Z. Li, Z. Xiao, H. Luo, X. Yuan, D. Zhang, Optimization of polarization direction on 3D printed 3-3 piezoelectric composites for sensing application, Addit. Manuf. 58 (2022) 103060, https://doi.org/10.1016/j.addma.2022.103060.

[11] H. Cui, R. Hensleigh, D. Yao, D. Maurya, P. Kumar, M.G. Kang, S. Priya, X. Zheng, Three-dimensional printing of piezoelectric materials with designed anisotropy and directional response, Nat. Mater. 18 (2019) 234–241, https://doi.org/10.1038/s41563-018-0268-1.

[12] G. Miao, W. Du, M. Moghadasi, Z. Pei, C. Ma, Ceramic binder jetting additive manufacturing: effects of granulation on properties of feedstock powder and printed and sintered parts, Addit. Manuf. 36 (2020) 101542, https://doi.org/10.1016/j.addma.2020.101542.

[13] M. Mariani, G.F. Blanco, E. Mercadelli, A.J. Sánchez-Herencia, C. Galassi, N. Lecis, B. Ferrari, Tailoring α-alumina powder morphology through spray drying for cold consolidation by binder jetting, Open Ceram 12 (2022) 100307, https://doi.org/10.1016/j.oceram.2022.100307.

[14] Q. Chen, E. Juste, M. Lasgorceix, F. Petit, A. Leriche, Binder jetting process with ceramic powders: influence of powder properties and printing parameters, Open Ceram 9 (2022) 100218, https://doi.org/10.1016/j.oceram.2022.100218.

[15] V. Sufiiarov, A. Kantyukov, A. Popovich, A. Sotov, Synthesis of spherical powder of lead-free BCZT piezoceramics and binder jetting additive manufacturing of triply periodic minimum surface lattice structures, Materials (Basel) 15 (2022) 6289, https://doi.org/10.3390/ma15186289.

[16] M. Mariani, R. Beltrami, P. Brusa, C. Galassi, R. Ardito, N. Lecis, 3D printing of fine alumina powders by binder jetting, J. Eur. Ceram. Soc. 41 (2021) 5307–5315, https://doi.org/10.1016/j.jeurceramsoc.2021.04.006.
[17] F. Bertolini, M. Mariani, E. Mercadelli, C. Baldisserri, C. Galassi, C. Capiani, R. Ardito, N. Lecis, 3D printing of potassium sodium niobate by binder jetting: printing parameters optimisation and correlation to final porosity, J. Mater. Res. Technol. 29 (2024) 4597–4606, https://doi.org/10.1016/j.jmrt.2024.02.145.
[18] M. Venet, W. Santa-Rosa, J.C. M'Peko, H. Amorín, M. Algueró, R. Moreno, Controlling colloidal processing of (K,Na)NbO3-based materials in aqueous medium, J. Eur. Ceram. Soc. 39 (2019) 3456–3461, https://doi.org/10.1016/j.jeurceramsoc.2019.02.026.
[19] A. Mahajan, R. Pinho, M. Dolhen, M.E. Costa, P.M. Vilarinho, Unleashing the full sustainable potential of thick films of lead-free potassium sodium niobate (K 0.5 Na 0.5 NbO 3) by aqueous electrophoretic deposition, Langmuir 32 (2016) 5241–5249, https://doi.org/10.1021/acs.langmuir.6b00669.
[20] R. Ladj, T. Magouroux, M. Eissa, M. Dubled, Y. Mugnier, R. Le Dantec, C. Galez, J.-P. Valour, H. Fessi, A. Elaissari, Aminodextran-coated potassium niobate (KNbO3) nanocrystals for second harmonic bio-imaging, Colloids Surfaces A Physicochem. Eng. Asp. 439 (2013) 131–137, https://doi.org/10.1016/j.colsurfa.2013.02.025.
[21] M. Rotan, M. Zhuk, J. Glaum, Activation of ferroelectric implant ceramics by corona discharge poling, J. Eur. Ceram. Soc. 40 (2020) 5402–5409, https://doi.org/10.1016/j.jeurceramsoc.2020.06.058.
[22] M. Mariani, R. Beltrami, E. Migliori, L. Cangini, E. Mercadelli, C. Baldisserri, C. Galassi, N. Lecis, Additive manufacturing of lead-free KNN by binder jetting, J. Eur. Ceram. Soc. 42 (2022) 5598–5605, https://doi.org/10.1016/j.jeurceramsoc.2022.05.075.
[23] J.I. Roscow, J. Taylor, C.R. Bowen, Manufacture and characterization of porous ferroelectrics for piezoelectric energy harvesting applications, Ferroelectrics 498 (2016) 40–46, https://doi.org/10.1080/00150193.2016.1169154.
[24] R.W.C. Lewis, A.C.E. Dent, R. Stevens, C.R. Bowen, Microstructural modelling of the polarization and properties of porous ferroelectrics, Smart Mater. Struct. 20 (2011) 085002, https://doi.org/10.1088/0964-1726/20/8/085002.
[25] J.B. Lim, S. Zhang, H.J. Lee, J. Jeon, T.R. Shrout, Shear-mode piezoelectric properties of modified-(K,Na)NbO 3 ceramics for "hard" lead-free materials, J. Am. Ceram. Soc. 93 (2010) 2519–2521, https://doi.org/10.1111/j.1551-2916.2010.03870.x.
[26] S. Zhang, R. Xia, T.R. Shrout, G. Zang, J. Wang, Piezoelectric properties in perovskite 0.948(K0.5Na0.5)NbO3–0.052LiSbO3 lead-free ceramics, J. Appl. Phys. 100 (2006), https://doi.org/10.1063/1.2382348.
[27] Y. Liu, L. Bian, R. Zhang, J. Fan, D. Huo, B. Shen, H. Huang, X. Shi, D. Wang, K. Yao, Ultrahigh electromechanical response in (K,Na)NbO3-based lead-free textured piezoceramics, Appl. Phys. Rev. 11 (2024), https://doi.org/10.1063/5.0224215.